applied sciences

MDPI

Article

Strontium Ferromolybdate-Based Magnetic Tunnel Junctions

Gunnar Suchaneck [1,*], Evgenii Artiukh [1,2], Nikolai A. Sobolev [3,4], Eugene Telesh [5], Nikolay Kalanda [2,4], Dmitry A. Kiselev [6], Tatiana S. Ilina [6] and Gerald Gerlach [1]

1 Solid-State Electronics Laboratory, TU Dresden, 01062 Dresden, Germany; sirfranzferdinand@yandex.ru (E.A.); gerald.gerlach@tu-dresden.de (G.G.)
2 Cryogenic Research Division, SSPA "Scientific-Practical Materials Research Centre of NAS of Belarus", 220072 Minsk, Belarus; kalanda362@gmail.com
3 i3N and Departamento de Física, Universidade de Aveiro, 3810-193 Aveiro, Portugal; sobolev@ua.pt
4 Laboratory of Functional Low-Dimensional Structures, National University of Science and Technology "MISIS", 4 Leninskiy Prospect, 119049 Moscow, Russia
5 Department of Electronic Technology and Engineering, Belarusian State University of Informatics and Radioelectronics, 6 P. Brovky Str., 220013 Minsk, Belarus; etelesh@mail.ru
6 Laboratory of Physics of Oxide Ferroelectrics, Department of Materials Science of Semiconductors and Dielectrics, National University of Science and Technology "MISiS", 4 Leninskiy Prospekt, 119049 Moscow, Russia; dm.kiselev@misis.ru (D.A.K.); ilina.tatina@gmail.com (T.S.I.)
* Correspondence: gunnar.suchaneck@tu-dresden.de

Abstract: Thin-film strontium ferromolybdate is a promising material for applications in room-temperature magnetic tunnel junction devices. These are spin-based, low-power-consuming alternatives to CMOS in non-volatile memories, comparators, analog-to-digital converters, and magnetic sensors. In this work, we consider the main tasks to be solved when creating such devices based on strontium ferromolybdate: (i) selecting an appropriate tunnel barrier material, (ii) determining the role of the interface roughness and its quantification, (iii) determining the influence of the interface dead layer, (iv) establishing appropriate models of the tunnel magnetoresistance, and (v) promoting the low-field magnetoresistance in (111)-oriented thin films. We demonstrate that (i) barrier materials with a lower effective electronegativity than strontium ferromolybdate are beneficial, (ii) diminution of the magnetic offset field (the latter caused by magnetic coupling) requires a wavy surface rather than solely a surface with small roughness, (iii) the interface dead-layer thickness is of the order of 10 nm, (iv) the tunnel magnetoresistance deteriorates due to spin-independent tunneling and magnetically disordered interface layers, and (v) antiphase boundaries along the growth direction promote the negative low-field magnetoresistance by reducing charge carrier scattering in the absence of the field.

Keywords: magnetic tunnel junction; strontium ferromolybdate; tunnel barrier material; surface roughness; interface layers; tunnel magnetoresistance

check for updates

Citation: Suchaneck, G.; Artiukh, E.; Sobolev, N.A.; Telesh, E.; Kalanda, N.; Kiselev, D.A.; Ilina, T.S.; Gerlach, G. Strontium Ferromolybdate-Based Magnetic Tunnel Junctions. *Appl. Sci.* **2022**, *12*, 2717. https://doi.org/10.3390/app12052717

Academic Editor: Victor Rouco

Received: 26 January 2022
Accepted: 2 March 2022
Published: 5 March 2022

Publisher's Note: MDPI stays neutral with regard to jurisdictional claims in published maps and institutional affiliations.

Copyright: © 2022 by the authors. Licensee MDPI, Basel, Switzerland. This article is an open access article distributed under the terms and conditions of the Creative Commons Attribution (CC BY) license (https://creativecommons.org/licenses/by/4.0/).

1. Introduction

Strontium ferromolybdate ($Sr_2FeMoO_{6-\delta}$—SFMO) double perovskites are promising candidates for magnetic electrode materials for room temperature (RT) spintronics applications because they present a half-metallic character (with theoretically 100% polarization), a high Curie temperature (T_C) of about 415 K (ferromagnets should be operated in their ordered magnetic state below T_C), and low-field magnetoresistance (LFMR) [1].

A magnetic tunnel junction (MTJ) consists of two ferromagnetic (FM) or ferrimagnetic layers separated by a thin insulator serving as a tunneling barrier. One of the magnetic layers (the pinned layer) has its magnetization direction fixed, e.g., by exchange bias, while the magnetization direction in the other layer (the free layer) can be changed by applying a magnetic field or injecting a spin-polarized current. If the two magnetizations have parallel orientations, electrons will tunnel through the insulating layer, and the device is in the

low-resistance state. If they have antiparallel orientations, practically no tunneling occurs (the high-resistance state) when one of the spin states, spin-up or spin-down, is dominating at the Fermi level. Consequently, such a junction can be switched between two states of electrical resistance.

A first attempt to fabricate SFMO-based MTJs was reported in [2]. A thin insulating layer covering the SFMO/$SrTiO_3$ surface was subjected to resistance-controlled nanoindentation. The indentation was stopped exactly when the tip reached the $SrTiO_3$ (STO) surface by controlling the resistance between the tip and the electrode underlying SFMO in real time and comparing it to the reference resistance measured before the lithography process. The indented holes were then filled up with Co, and thus a tunnel nanojunction was formed. Transport measurements revealed a positive tunnel magnetoresistance (TMR) of about 50% at 4 K. In a next attempt, a 50 × 50 μm^2 SFMO/STO/$CoFe_2O_4$ junction was fabricated [3]. The structure showed the behavior of a usual metal/insulator/semiconductor diode; TMR was absent. The same group has manufactured 50 × 50 μm^2 SFMO/STO/$CoFe_2$ tunnel junctions that did not show any magnetoresistance (MR) at 5 K [4]. In both cases, the absence of MR was assigned to an iron deficiency at the SFMO surface established by X-ray photoemission spectroscopy. MTJs with an area of 30 × 30 μm^2 were fabricated by means of SFMO thin films deposited on $Ba_{0.4}Sr_{0.6}TiO_3$-buffered STO substrates [5]. Native $SrMoO_4$ oxide formed by surface oxidation was used as a tunneling barrier, and a 50 nm thick Co film shunted by Au served as a counter-electrode. Junction delineation was carried out using standard UV lithography and ion milling. The structure possessed a TMR of 10% at 4.2 K. MTJs consisting of two SFMO electrodes separated by an STO barrier were described in [6,7]. Trilayer SFMO/STO/SFMO MTJ devices of 40 × 40 μm^2 area were created on an STO buffered Si (100) wafer. The large TMR of ~7% of the devices obtained at RT was ascribed to spin-dependent tunneling through the sufficiently thin (~2 nm) STO barrier. A comprehensive review of manganite-based magnetic tunnel structures [8] addressed the application of combined external factors (transport current, magnetic and electric fields, microwave and optical radiation) as well as comparing current-perpendicular-to-plane and current-in-plane geometries. However, $La_{0.7}Sr_{0.3}MnO_3$ thin films undergo a transition to the ferromagnetic state already at about 300 K. The discovery of the coherent tunneling effect at the Fe(100)/MgO(100) boundary, enabling theoretically MR values up to 1000% [9], shifted the research activities in recent years to MTJs employing magnetic electrodes of Fe-containing alloys.

In this work, we consider (i) selection of an appropriate tunnel barrier material, (ii) role of the interface roughness and its quantification, (iii) influence of the magnetic dead layer (DL) at the surface/interface, (iv) appropriate models of the TMR, and (v) microstructural promotion of the LFMR. We demonstrate that (i) barrier materials with effective electronegativity lower than that of SFMO are beneficial, (ii) diminution of the magnetic offset field (the latter caused by magnetic coupling due to interfacial roughness) requires a wavy rather than solely a smooth surface, (iii) the DL has a thickness in the order of 10 nm, (iv) the TMR deteriorates due to spin-independent tunneling and magnetically disordered interface layers, and (v) antiphase boundaries along the growth direction promote negative LFMR by reducing charge carrier scattering in the absence of the field.

2. Theoretical Considerations

2.1. Effective Electronegativity of Complex Oxide Compounds

Considering an ideal conductor-dielectric interface without surface- or adsorbate-induced states, a charge transfer occurs between the constituents, thus creating an interface dipole that shifts the relative position of the metal Fermi level with respect to the conduction and valence bands of the dielectric. The magnitude of the interface dipole is defined by the ability of both interface constituents to attract electrons, i.e., by their effective electronegativities. The Pauling electronegativity scale X is based on the difference between the actual and the expected bond formation enthalpy in various A-B molecules. The difference is attributed to the partially ionic character of the A-B bond. To set up relative

values for all elements, a value of $X = 4.0$ was assigned to the most electronegative element fluorine [10]. Similarly, the electron displacement at the interface occurs toward the more electronegative compound, i.e., it depends on the effective electronegativities $\langle X \rangle$ of the interface constituents. An appropriate way to calculate the effective electronegativity of materials consisting of N components is to use the geometric mean of the electronegativities of the constituent elements [11,12].

$$\langle X \rangle = \left(\prod_{i=1}^{N} X_i \right)^{1/N} \tag{1}$$

The effective electronegativity, Equation (1), is correlated with the work function of metal, carbide, oxycarbide, nitride, oxynitride, and LaB_6 electrodes on HfO_2 [13], proving its suitability to characterize the charge exchange at electrode-dielectric interfaces.

2.2. Néel Coupling at the Interface

The tunnelling probability exponentially varies with the barrier thickness. Consequently, conformal coating of the bottom SFMO layer by a thin barrier layer is required. In this case, the Néel coupling—also called the "orange-peel" effect—appears due to nonzero surface roughness. Let us consider a laminar structure consisting of two FM layers, a fixed (pinned) layer and a free one, separated by a nonmagnetic barrier (NB) of thickness d_b, with conformal waviness described by a two-dimensional (2D) sinusoidal wave with a wavelength λ and amplitude h. Then, a magnetic offset field occurs in the free layer due to the magnetostatic coupling between the two in-plane polarized FM layers. In this case, a bulk, pinned hard-magnetic (HM) layer couples via the barrier to another bulk, free soft-magnetic (SM) layer. Accounting only for the first-order terms of h/d_g, with d_g being the grain size, the coupling field is given in the limit of rigid isotropic in-plane magnetization by [14,15]:

$$H_{off} = \frac{\pi^2}{\sqrt{2}} \frac{h^2}{\lambda d_s} M_h \exp\left(-\frac{2\pi\sqrt{2} d_b}{\lambda} \right) \tag{2}$$

where d_s is the thickness of the SM layer and M_h is the magnetization of the HM layer. In thin-film structures, magnetic poles created at the outer surfaces of the magnetic layers result in additional FM and anti-FM interactions which must be taken into account. This yields an SM/NB/HM trilayer structure [16]:

$$\begin{aligned} H_{off} = {} & \frac{\pi^2 h^2 M_h}{\sqrt{2}\lambda d_s} \exp\left(-\frac{2\pi\sqrt{2} d_b}{\lambda} \right) \times \\ & \times \left[1 - \exp\left(-\frac{2\pi\sqrt{2} d_s}{\lambda} \right) \right] \cdot \left[1 - \exp\left(-\frac{2\pi\sqrt{2} d_h}{\lambda} \right) \right]. \end{aligned} \tag{3}$$

Experimentally, the inverse variation of H_{off} with the SM layer thickness and its exponential variation with the NB thickness were observed in [17,18]. A coercivity enhancement in the free layer resulting from the orange-peel coupling was reported in [19]. Note that small offset fields require $h << \lambda$. In this case, both pulsed laser deposition (PLD) and magnetron sputtering (MSP) ensure conformal surface coating. PLD generates short time (μs) fluxes of condensable species with large kinetic energies (a few eV up to several tens eV) [20]. This favors layer-by-layer growth and, therefore, film crystallinity and conformal edge coverage. Moreover, film growth is not disturbed by new incident species between the laser pulses. As a result, additional surface diffusion occurs. MSP is a deposition method possessing a more directed flux of film-forming species. Here, DC pulsing in the kHz range is convenient for suppressing arc formation. Ions with energies up to several hundred eV are impinging on the growing film surface [21], providing a layer-by-layer growth with $h << \lambda$ and a widely conformal substrate coverage at low incident fluxes. A review of SFMO film deposition and post-processing is provided in [22].

The case of uniform out-of-plane magnetization of the two FM layers was considered in [23]. Here, the magnetostatic anisotropy constant with an absolute value up to

$|K| = 1.32 \times 10^6$ J/m^3 will be negative, corresponding to a parallel alignment of the magnetizations in the two FM layers. The out-of-plane magnetization induces an anti-FM interaction between the layers due to a stray field resulting from the uniformly charged curved surface [24]. For arbitrary orientations of magnetization, the offset field is given by [24]:

$$\begin{aligned} H_{off} &= \frac{\pi^2 h^2}{\sqrt{2}\lambda d_s} M_h \exp\left(-\frac{2\pi\sqrt{2}d_b}{\lambda}\right) \times \\ &\times \left[1 - \exp\left(-\frac{2\pi\sqrt{2}d_s}{\lambda}\right)\right] \cdot \left[1 - \exp\left(-\frac{2\pi\sqrt{2}d_h}{\lambda}\right)\right] \times \\ &\times (2\sin\alpha\sin\beta - \cos\alpha\cos\beta), \end{aligned} \tag{4}$$

where α and β are the angles between the magnetization and the average interface. Appropriate values of h and λ can be derived by means of atomic force microscopy (AFM).

A surface topography scan provides a root-mean-square (RMS) surface roughness R_{rms} as the average of the measured height deviations taken over N points and measured from the mean line $\langle h \rangle$:

$$R_{\mathrm{rms}} = \sqrt{\frac{1}{N}\sum_{n=1}^{N}(h_n - \langle h \rangle)^2} \tag{5}$$

A more comprehensive characterization uses the power spectral density (PSD) function. It represents the square of the Fourier spectrum of the surface profile. Thus, it contains all information about both the vertical and the lateral structures. Current software for SPM data visualization and analysis, e.g., Gwyddion [25], includes the calculation of 1D (line scans) or 2D (area scans) PSDs [26]:

$$PSD_{2-D}(f) = \frac{PSD_{1-D}(f)}{2\pi f}, \tag{6}$$

with f being the frequency of spatial waves. For the 1D case, the RMS amounts to

$$R_{RMS} = \sqrt{\int_{f_1}^{f_2} PSD(f)df}. \tag{7}$$

A mathematical PSD model allows the removal of algorithmic procedure artifacts related to finite bandwidth, discrete spatial frequencies, and fluctuations. The k-correlation model (also called the ABC model) [27,28],

$$PSD_{ABC} = \frac{A}{(1 + B^2 f^2)^{C/2}}, \tag{8}$$

characterizes a 1D PSD of a self-affine and perfectly isotropic surface not affected by the substrate. The parameter A describes the low-frequency limit of the spectrum. The physical meaning of the flat part of this curve at low frequencies is that across these dimensions in real space, there is no significant deviation in the height value. Therefore, parameter B defines a correlation length $l_c = B/2\pi$, beyond which the surface height fluctuations are not correlated. Hence, B represents a mean grain size. The parameter C depends on the growth mechanism [29]. Correspondingly, R_{rms} is given by [28]:

$$R_{RMS} = \frac{\sqrt{\pi}\cdot\Gamma(C + 1/2)}{\Gamma(C/2)} \frac{AB}{(C-1)B^2}. \tag{9}$$

In the following equation, we equate R_{RMS} to the waviness amplitude h. The average spatial wavelength will be defined using the half-maximum amplitude criterion. Then, $\langle \lambda \rangle$ corresponds to the spatial wavelength at $A/6\mathrm{dB} \approx A/4$. The average spatial wavelengths determined in this way are in good agreement with the average of multiple line scans calculated as in [30]

$$\langle \lambda \rangle = 1/\ln\left[\frac{1}{N}\sum_{n=1}^{N}\exp(-1/\lambda_n)\right]. \quad (10)$$

2.3. Interface Dead Layer

The magnetic properties of ultrafine granular systems are size-dependent. FM properties appear when the layer thickness exceeds a critical value denoted as a dead layer (DL). For instance, a drastic drop in the magnetization, when the particle size of $La_{0.8}Sr_{0.2}MnO_{3-\delta}$ nanoparticles decreases to 8 nm, indicates the formation of a DL at the surface [31]. The thickness of this DL was found to have a logarithmic dependence on the particle size. In $La_{0.7}Sr_{0.3}MnO_3$/depleted manganite/MnSi/SiO_2 structures, DL formation at the upper interface is avoided by using the depleted manganite layer as a tunneling barrier [8]. A similar DL was obtained in metallic Fe [32] and Ni films [33], both deposited by electroplating onto Cu, Ag or Au substrates. The existence of such DLs at $T = 0$ was attributed to a transfer of electrons from the *s*-band to the *d*-band in the neighborhood of a surface, thus affecting the magnetic moment. A special form of a dead layer is a magnetically disordered layer.

The magnetization averaged over the film thickness in the presence of a DL amounts to [33]

$$M = M_{bulk}\left(1 - \frac{\delta}{d}\right), \quad (11)$$

where δ is the DL thickness and d is the film thickness. In [34], the DL at the surface of Fe nanoparticles was assigned to a 1 to 2 nm thick coating with Fe oxides. DLs related to a distorted structure near the surface were also found in thin films of yttrium-iron garnet [35] and $DyTiO_3$ [36], both deposited by PLD. In the latter case, the DL with a thickness of 4–5 nm was located at the film surface where magnetic Ti^{3+} ions are replaced by nonmagnetic Ti^{4+} ions, leading to a paramagnetic response. In the case of FM $La_{0.7}Sr_{0.3}MnO_3$ (LSMO) thin films grown by PLD, interfacial DLs were formed due to phase separation [37]. They had a thickness of 3–5 nm, 3–5 nm, and 5–8 nm for films grown on STO (001), $NdGaO_3$ (110) and $LaAlO_3$ (001) substrates, respectively. On the other hand, LSMO films deposited by PLD onto STO (001) with thicknesses ranging from 3 to 70 unit cells exhibited a reduction of the saturation magnetization below a thickness of 4.8 nm, a thickness of a nonmetallic interface layer of 3.2 nm, and vanishing of ferromagnetism below 1.2 nm [38]. The difference in the critical thicknesses to produce ferromagnetism and metallicity was explained by phase separation into FM/metallic and non-FM/nonmetallic regions with a loss of percolation at a critical thickness. A recent study of PLD deposited LSMO thin films revealed a dependence of the δ parameter on the oxygen pressure p_{O2} during film growth, with δ ranging from 2.4 nm for 0.05 Pa to 1.1 nm for 26.6 Pa [39].

2.4. Tunnel Magnetoresistance

The TMR of FM/insulator/FM tunnel junctions can be qualitatively described by means of the Jullière model [40]. The model considers tunneling between magnetically aligned and anti-aligned electrodes. Thereby, the spin is supposed to be conserved. Assuming the same matrix element for the tunneling of the majority and minority spin electrons, the TMR between these configurations arises from the degree of spin polarization P of the carriers [8]:

$$P = \frac{n_\uparrow(E_F) - n_\downarrow(E_F)}{n_\uparrow(E_F) + n_\downarrow(E_F)} \quad (12)$$

where $n_{\uparrow(\downarrow)}(E_F)$ is the density of states of spin-up (spin-down) electrons at the Fermi level E_F. Defining the TMR as

$$TMR = \frac{R_{AP} - R_P}{R_P}, \quad (13)$$

where R_{AP} is the electrical resistance in the anti-parallel and R_P is that in the parallel state, the TMR is given in terms of the degrees of the conduction electron spin polarization P_1 and P_2 in the two magnetic layers as:

$$TMR = \frac{2P_1P_2}{1 - P_1P_2}. \quad (14)$$

The spin polarization resembles the spontaneous magnetization behavior at low temperatures known as Bloch's $T^{3/2}$ law [41]:

$$P(T) = P_0(1 - \alpha T^{3/2}). \quad (15)$$

Here, α is a fitting parameter that is generally larger for the surface than for the bulk magnetization [42], being very sensitive to surface contaminants [43]. The TMR is then determined by [44]:

$$TMR = \frac{2P_0^2(1 - \alpha T^{3/2})^2}{1 - P_0^2(1 - \alpha T^{3/2})^2}. \quad (16)$$

Assuming tunneling via a magnetically disordered layer at the interface possessing angles between the spin orientation at the interface and the magnetization in the range of 0 to π, Equation (16) becomes:

$$TMR = \frac{2P_0^2(1 - \alpha T^{3/2})^2}{3 - P_0^2(1 - \alpha T^{3/2})^2}. \quad (17)$$

In this case, the TMR estimated for SFMO lowers to about 6%, slightly smaller than the experimental value [6].

The combined action of inelastic spin-independent tunneling and tunneling via a magnetically disordered layer at the interface may be expected in the presence of iron-deficient interface layers [3,4].

If one takes into account the transmission probability by tunneling, one has to replace the FM polarization with the effective spin polarization of the FM–barrier couple [45]:

$$P_{fb} = \frac{(k_\uparrow - k_\downarrow)}{(k_\uparrow + k_\downarrow)} \cdot \frac{(\kappa^2 - k_\uparrow k_\downarrow)}{(\kappa^2 + k_\uparrow k_\downarrow)}, \quad (18)$$

where κ is the reciprocal localization length of the wave function inside the barrier:

$$\kappa = \sqrt{\frac{2m_e^* V_0}{\hbar^2}}. \quad (19)$$

Here m_e* is the effective electron mass, V_0 is the barrier height, $\hbar$ is the Planck constant expressed in J·s/radian, and $k_{\uparrow(\downarrow)}$ is the wave vector of the wave function of the tunneling spin-up (spin-down) electrons. Thus, theory [45] predicts a decrease in spin polarization with barrier height. With regard to Equation (16), the Jullière model [40] then represents the limit of a very small wavefunction overlap, i.e., it is valid for sufficiently thick barriers.

SFMO is half-metallic where only spin-down states should be active at the Fermi surface (100% spin polarization) [1]. In this case, $k_\uparrow$ becomes imaginary, and the MTJ represents a perfect magnetic valve with zero conductivity for antiparallel spin orientation in the two ferromagnetic layers. On the other hand, the calculation of $k_\downarrow$ for SFMO is cumbersome. For FM Fe, the Fermi surface of the itinerant d_i-electrons can be approximated by a sphere of radius $k_F = (3\pi n_e)^{1/3}$, where n_e is the total electron density [46]. The Fermi surfaces of lanthanum manganite A-site substituted by one-third of divalent ions [47], as well as SFMO [48], are more complicated, thus hindering precise analytical calculations of $k_\downarrow$.

2.5. Low-Field Magnetoresistance

In LSMO ceramics, extrinsic LFMR was found in 1996 [49]. It was shown that the MR in polycrystalline LSMO exhibits two distinct regions: large MR at low fields (~0.1 T) dominated by spin-dependent tunneling between grains, and high-field MR also obtained in single crystals. However, the initial expectation of using LSMO in RT spintronic applications was not fulfilled. Two years later, the discovery by Kobayashi et al. in 1998 [1] of LFMR and the half-metallicity of SFMO possessing a Curie temperature of about 420 K renewed the interest in double perovskites in the context of their potential applications in the field of spin electronics.

At present, it is well established that the main contribution to LFMR in SFMO ceramics arises from spin-dependent electron tunneling across insulating grain boundaries (GBs) [50–52] and not from the existence of Fe/Mo antisite defects (ASD) in the bulk [53]. The LFMR is almost absent in single crystals [54]. A study of an epitaxial SFMO thin film grown on an STO (100) bicrystal boundary has proven that LFMR is caused by spin-dependent electron transfer across GBs and not by an intragranular effect [55]. Depending on deposition conditions, LFMR might be missing in SFMO thin films deposited by PLD onto STO (001) substrates [56,57]. However, the tunneling barriers necessary for LFMR could be additionally created, e.g., by a post-deposition heat treatment at 475–500 °C in an ultrapure Ar (99.9995 %) atmosphere for 5 h [56] or by annealing in a reducing $5\%H_2/N_2$ atmosphere for 10 h at 950 °C [58]. In comparison, neither magnetic nor magnetotransport nor structural properties were improved by post-deposition annealing of SFMO thin films at temperatures between 500 and 1100 °C in a vacuum, Ar, $5\%H_2/Ar$, or air atmospheres for 5 or 10 h [59]. Obviously, grain boundary modification should be performed under carefully selected conditions.

SFMO thin films grown by PLD on STO (111) substrates exhibit a larger LFMR effect in (111)-oriented films compared to those with the (001) orientation [60]. The origin of this phenomenon is suggested to be the presence of antiphase domain boundaries (APBs). In fact, APBs are nucleated at steps on the substrate surfaces if nucleation on the two terraces separated by a step edge starts at different atomic planes [61]. Atomically flat STO (111) surfaces show a clear step-and-terrace structure with a step height of about 0.24 nm [62]. This approximately corresponds to the plane separation d_{111} = 0.228 nm of SFMO in the (111) direction [63]. Note that the larger separation of (111) planes at the substrate surface favors the formation of FeO_6–FeO_6 octahedra in comparison to FeO_6–MoO_6 octohedra. Experimentally, a step height of about 0.45 nm was derived from AFM images on the surface of epitaxial (111)-oriented SFMO films obtained by growth mediated by screw dislocations on STO (111) substrates [60]. This value corresponds to $2d_{111}$ and provides evidence that film growth takes place with a unit cell as a growth species.

The LFMR is favored in thin films subjected to large biaxial compressive strain at the film-substrate interface [57]. This was related to the formation of low-angle GBs.

3. Results and Discussion

3.1. Selection of Tunneling Barrier Material Based on Electronegativity Differences

The first challenge is the appropriate selection of barrier material. Tunneling is affected by the properties of the electrode/barrier interface. For instance, the interfacial spin polarization of $La_{2/3}Sr_{1/3}MnO_3$ deposited onto various barrier materials ($SrTiO_3$, TiO_2, $LaAlO_3$) significantly depends on the barrier material and is strongly different from the spin polarization of a free surface [64]. On the other hand, suppression of both the Curie temperature T_C and magnetization was observed in a $La_{0.7}Ca_{0.3}MnO_3$/STO superlattice as the thickness of the $La_{0.7}Ca_{0.3}MnO_3$ layer decreased, which was attributed to interfacial magnetic disorder [65].

In half-metallic SFMO, only the spin-down (minority) band is present at the Fermi level providing 100% spin polarization [1]. This leads to a negative spin polarization that is characterized by a higher tunneling probability for minority spin electrons [2]. Around the Fermi level, the spin-down band is occupied by both the Mo 4*d* t_{2g} and the Fe 3*d* t_{2g}

electrons, which are strongly hybridized with the oxygen 2*p* states [1]. Here, the attraction of a larger part of the electron density to the SFMO side of the interface increases the occupation of the spin-down states by electrons near the interface (Figure 1).

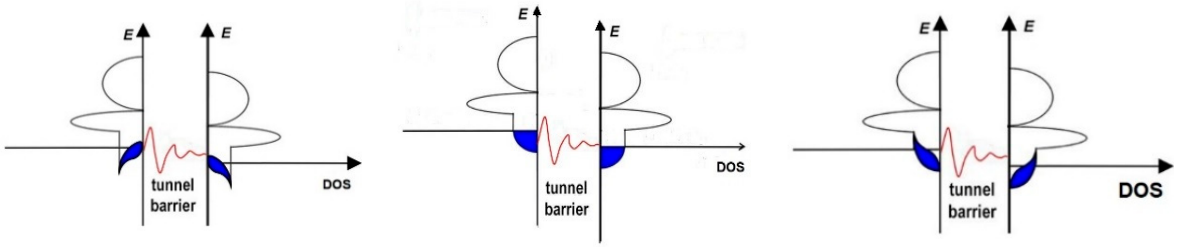

(**a**) (**b**) (**c**)

Figure 1. Tunneling FM/barrier/FM for $X_{SFMO} > X_{barrier}$ (**a**), $X_{SFMO} = X_{barrier}$ (**b**), and $X_{SFMO} < X_{barrier}$ (**c**). Energy is plotted along the vertical axis, and the density of states of the FM layers is plotted along the horizontal axis. Filled states are shown in blue. A negative bias voltage, V, has been applied to the sample, which effectively raises its Fermi level by $e \cdot V$ with respect to the Fermi level of the grounded FM electrode.

The effective electronegativities of FM electrode materials, as well as of potential barrier materials, calculated using Equation (1), are compiled in Table 1.

Table 1. Effective electronegativities of ferro and FM electrode materials, as well as of potential barrier materials.

Compound	Function	<X>
Fe	Electrode	1.83
NiFe	Electrode	1.87
Co	Electrode	1.88
MgO	Barrier	2.12
La_2O_3	Barrier	2.18
$BaTiO_3$	Barrier	2.24
$SrTiO_3$	Barrier	2.26
$Ce_{0.69}La_{0.31}O_{1.845}$	Barrier	2.31
$La_{2/3}Sr_{1/3}MnO_3$	Electrode	2.31
$La_{0.7}Sr_{0.3}MnO_3$	Electrode	2.31
$LaAlO_3$	Barrier	2.35
ZnO	Barrier	2.38
Sr_2FeMoO_6	Electrode	2.38
$Mg_3B_2O_6$	Barrier	2.40
$SrMoO_3$	Barrier	2.42
HfO_2	Barrier	2.49
Mn_2O_3	Barrier	2.50
Al_2O_3	Barrier	2.54
$SrMoO_4$	Barrier	2.57
Fe_3O_4	Electrode	2.62
TiO_2	Barrier	2.63
MnO_2	Barrier	2.64
Ta_2O_5	Barrier	2.71

The attraction of more electrons to the SFMO side of the interface stems from the higher X value of SFMO compared to that of the barrier. This can compensate in part for the weakening of magnetism due to interfacial magnetic disorder obtained in [65]. The opposite occurs for a barrier with a higher X value than that of SFMO. Consequently, barrier materials with a smaller electronegativity are beneficial for a high TMR. This is in agreement with the values of the TMR of $La_{2/3}Sr_{1/3}MnO_3$ on $SrTiO_3$, $LaAlO_3$, and TiO_2

barriers and a Co counter-electrode amounting to 540, 301, and 140%, respectively [64]. As a result, $SrTiO_3$, La_2O_3, and MgO are barrier materials suitable for SFMO.

It has to be noted that this simplified approach is valid for an ideal interface grown in a layer-by-layer mode, since the concept of effective electronegativity models the interface dipole between a dielectric and metal surface and does not take into account interface charges and defects. It is not consistent with a change of the layer-by-layer to the island growth [66], multiple phase separation into FM-metallic, FM-insulating, and non-FM-insulating regions at the interface of $La_{2/3}Ca_{1/3}MnO_3$ with $SrTiO_3$, $LaAlO_3$, and $NdGaO_3$ [67], as well as interlayer electron hopping through $SrTiO_3$ layers when the layer thickness is reduced to less than three unit cells [68]. In Section 2.2, it was shown that a layer-by-layer growth mode is potentially achievable by PLD and MSP. On the other hand, the approach in this section does not take into account additional oxygen or oxide layers influencing, e.g., the barrier transmission in Fe/MgO/Fe MTJs [69,70]. However, SFMO is an oxygen-deficient compound. Its further oxidation increases the saturation magnetization, i.e., it improves the interface quality [71].

The thickness of the barrier layer defines the resistance-area product $RA = dV/dJ$, with V being the applied voltage and J the current density [72]. It exponentially increases with barrier thickness where the slope yields the barrier height. Based on operational requirements on noise and access time, the RA product should be less than 10 $k\Omega \cdot \mu m^2$ [73]. Moreover, it should match the MTJ resistance to the resistance of path transistors, which is typically 10 kΩ. The RA product for parallel alignment of spins is almost independent of temperature, whereas for the antiparallel alignment it gradually decreases with temperature [74,75].

3.2. Evaluation of the Néel-Coupling Surface Characteristics

A second challenge is the surface waviness of thin films. We have characterized the surface morphology of the SFMO films by means of atomic force microscopy (AFM) (cf. Supplemental Materials, Figures S2 and S3). Figure 2 shows the 1D PSD of three different regions of an approximately 800 nm thick SFMO thin film (AFM images are depicted in Figure S2, Supplemental Materials) grown by multi-target reactive sputtering at 600 °C onto a 150 mm platinized silicon wafer in comparison with a fit to the k-correlation model, Equation (8). The initial RMS roughness of the Pt layer was 1.4 nm (cf. Supplemental Materials, Figure S1). The final RMS roughness of the SFMO thin film estimated using Equation (9) amounts to 13.6 nm, whereas the average spatial wavelength derived from the half-maximum amplitude criterion amounts to 217 nm. For d_h = 800 nm, d_b = 2 nm, and d_s = 4 nm, the relative offset field yields H_{off}/M_s = 0.15, which is not suitable for applications. This value can be reduced to H_{off}/M_s = 0.02 by reducing the surface roughness to 5 nm. On the other hand, samples deposited at RT onto STO substrates by ceramic target MSP and crystallized at about 900 °C at BGUIR (Minsk, Belarus) possess an RMS roughness of 35 nm and an average spatial wavelength of 1700 nm, yielding a ratio H_{off}/M_s = 0.016 (Figure 3, AFM images are depicted in Figure S3, Supplemental Materials).

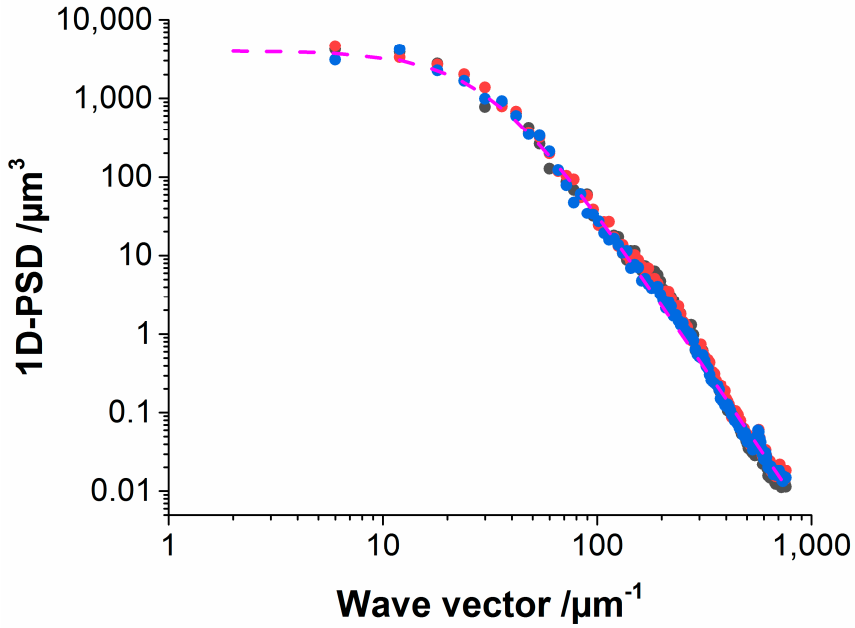

Figure 2. One-dimensional power spectral density of an SFMO thin film deposited by multi-target reactive sputtering at 600 °C (dots) in comparison with the ABC model, Equation (8) (dashed line). AFM scans were carried out at three different points with a scan area of 1.05 × 1.05 µm^2.

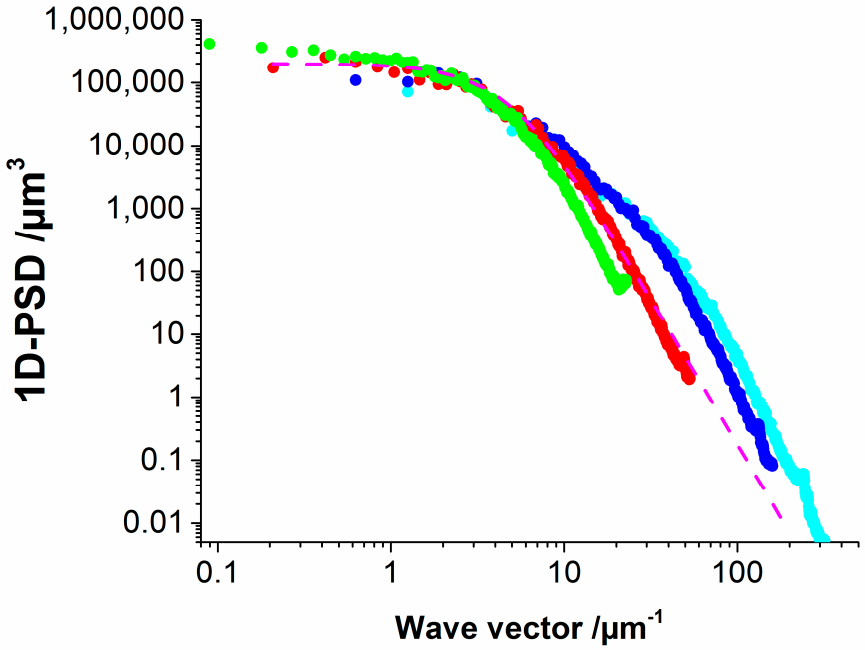

Figure 3. One-dimensional power spectral density of an SFMO thin film deposited by ceramic target magnetron sputtering and crystallized at 900 °C (dots) in comparison with the ABC model, Equation (8) (dotted line). AFM scans were carried out at one point using scanning areas of 5 × 5 µm^2 (light blue), 10 × 10 µm^2 (blue), 30 × 30 µm^2 (red) and 70 × 70 µm^2 (green).

3.3. Estimation of the Dead Layer Thickness of SFMO Thin Films

Unfortunately, most of the reports on SFMO thin film deposition are devoted to films with a thickness of about 100 nm [22]. To the best of our knowledge, there is only one report considering the thickness dependence of the saturation magnetization M_s of SFMO thin films deposited by PLD onto STO (001) and $(LaAlO_3)_{0.3}(Sr_2AlTaO_6)_{0.7}$ (001) (LSAT)

substrates [76]. Applying Equation (11) to this data, we find a total DL thickness (we are not able to distinguish between interface and surface layer) of 11 to 14 nm (Figure 4). This is in reasonable agreement with the values of nonmagnetic interface layers, obtained in $La_{2/3}Ca_{1/3}MnO_3$ thin films deposited by RF sputtering [77] and in PLD deposited $La_{0.67}Sr_{0.33}MnO_3$ thin films [78], amounting to 5.3 ± 0.9 nm and 4.6 ± 0.9 nm, respectively.

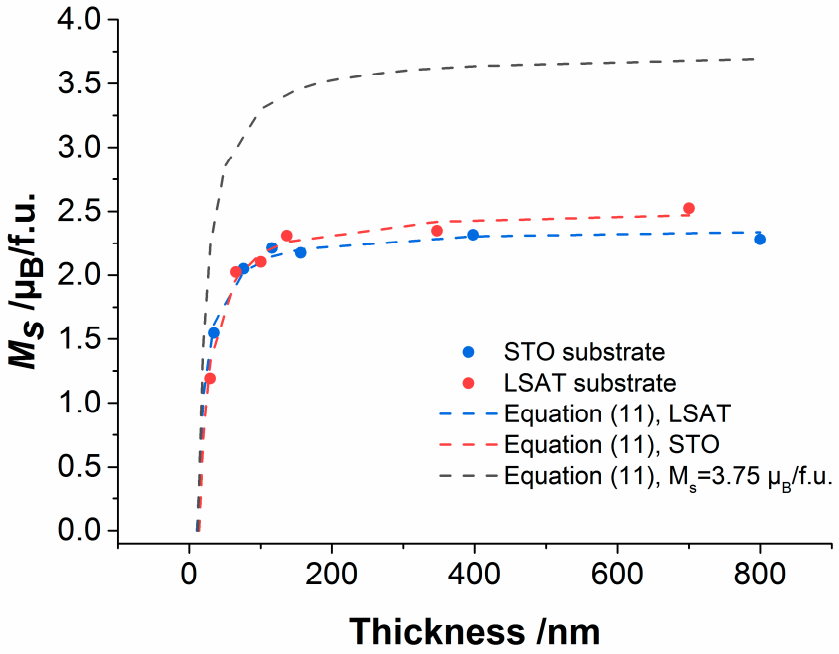

Figure 4. Thickness dependence of the saturation magnetization M_s of SFMO thin films measured in a magnetic field of 400 mT at 10 K [76] in comparison with the DL model (Equation (11)). Additionally, an outlook is given for high-quality SFMO thin films possessing a saturation magnetization of 3.75 μB/f.u.

On the other hand, there is evidence that the STO/$CoFe_2$ interface considered below is less problematic with respect to DLs. The DL is practically absent at Co/Cu interfaces [79]. High-quality epitaxial $CoFe_2O_4$ (CFO) with a magnetization near the bulk value can be prepared on STO despite the large lattice mismatch. Diffusion of the involved ions is not expected due to different ion sizes, crystallographic structures, and electron configurations [80]. In addition, the FM order in the DL at a CFO/Al_2O_3 interface is partially restored by increasing the CFO thickness d from 1.4 to 2.3 nm [81]. This restoration likely originates from an interlayer coupling of the DL at d = 1.4 nm with an additional 0.9-nm-thick CFO layer having a stronger FM ordering. This leads to a large slope of the magnetization-vs.-thickness curve at least up to d = 4 nm. Note that CFO is an insulating material that exhibits a half-metal-like behavior only in combination with a nonmagnetic electrode in a double spin-filter junction [82].

3.4. Attainable Tunnel Magnetoresistance

A spin-polarization value of P = 0.85 was deduced by means of the Jullière model for an SFMO/STO/Co junction at 4 K, where the SFMO possesses an antisite disorder parameter ASD = 0.15 [2]. The P values obtained for SFMO single crystals were 0.67 ± 0.03, 0.66 ± 0.02, and 0.59 ± 0.05 at T = 1.2 K for ASD amounting to 0.11, 0.15, and 0.16, respectively [83]. The spin-polarization values were found to be independent of temperature, which was anticipated in the considered temperature range from 1.2–3.76 K, well below the Curie temperature of SFMO. Taking into account data in [83], Equation (15) was approximated choosing P_0 = 0.9. Here, Equation (16) yields a zero-temperature TMR of about 430%. The parameter α determined using the data for $(Ba_{0.8}Sr_{0.2})_2FeMoO_6$ given in [84]

amounts to 1.31×10^{-4} $K^{-3/2}$, which is one order of magnitude larger than the values for Co, permalloy [41], NiFe [85], and $FeNiB_{0.5}$ [42,43], and about three times the value for $La_{2/3}Sr_{1/3}MnO_3$, but on the order of the values obtained for $La_{2/3}Sr_{1/3}MnO_3$ grown on various barrier materials ($SrTiO_3$, TiO_2, $LaAlO_3$). It amounts to about one-third of the value for the $La_{2/3}Sr_{1/3}MnO_3$ free surface [64]. Inserting the obtained α value of SFMO into Equation (15), we find P(298 K) = 0.293 and, correspondingly, using Equation (16), TMR(298 K) = 19%. For an SFMO(150 nm)/STO(2 nm)/SFMO(50 nm) MTJ device, an experimental value of TMR(298 K) ≈ 7% was reported in [6], corresponding to spin polarization of 18%. As for conventional tunnel junctions, the presence of defect states in the barrier reduces the MR [86]. Unpaired electrons will increase the spin-flip rate so that MR could vanish with increasing defect concentration. On the other hand, the discrepancy between experimental observation and direct spin-dependent tunneling theory can be overcome by additionally taking into account the spin-independent tunneling. One such tunneling mechanism is hopping through chains of N localized states resulting in additional conductivity that is temperature-independent for $N = 1$ and exhibits power laws $T^{4/3}$ and $T^{5/2}$ for $N = 2$ and $N = 3$, respectively [87]. This adds a correction to R_{AP}, yielding for $N = 2$ a TMR of [44]

$$TMR = \frac{2P_0^2(1-\alpha T^{3/2})^2 - \beta_{SI}(T)}{1 - P_0^2(1-\alpha T^{3/2})^2 + \beta_{SI}(T)}, \quad (20)$$

where $\beta_{SI}(T)$ is a coefficient, both temperature- and barrier-dependent, attributed to second-order inelastic tunneling that displays a conductivity contribution of $\sigma \propto T^{4/3}$. The room-temperature TMR of SFMO matches the experimental data described above [6] for β_{SI}(298 K) ≈ 0.1.

3.5. Promotion of the Low-Field Magnetoresistance in (111)-Oriented Thin Films

Let us consider the LFMO in (111)-oriented SFMO films comprising APBs. The electrical conductivity across APBs comes into play only in the presence of a magnetic field when the spins of all grains are oriented in the field direction [88]. On the other hand, the resistivity of (111)-oriented SFMO films is smaller than that of (100)-oriented ones by a factor of 2 to 3 lower [60]. Additionally, in the first case, the resistivity behavior is more similar to that of single crystals [54,89], which can be modelled by [89]

$$\rho(T) = \rho_0 + R \cdot T^2. \quad (21)$$

Here, ρ_0 is the residual metallic resistivity and R is a coefficient depending on the charge carrier scattering mechanism. The resistivity behavior of (111)-oriented SFMO thin films can be explained by the fact that APBs in (111)-oriented SFMO films are directed along the growth direction. Here, the APBs lead to the confinement of charge carriers within a domain. This increases the charge carrier scattering length. As a result, the ρ_0 value of SFMO decreases due to a larger scattering length. When a magnetic field is applied, the APBs become more penetrable for charge carriers, and their scattering length decreases. This gives an additional contribution to the LFMR.

4. Conclusions

The practical implementation of SFMO-based MTJs requires attention to a number of specific aspects:

- In the case of a lower effective electronegativity of the barrier material compared to SFMO, e.g., for MgO, La_2O_3, $BaTiO_3$, $SrTiO_3$, $LaAlO_3$, and ZnO, the attraction of more electrons to the SFMO side of the interface increases the occupation of the spin-down states by electrons near the interface. This increases the density of states at the Fermi level and, thus, the tunnel current.
- The magnetic offset field caused by magnetic coupling due to interfacial waviness is determined not only by the surface roughness (amplitude of spatial waves) but also by the width or spacing of surface features (wavelength of spatial waves). A slowly

changing surface profile corresponding to a wavy surface rather than a rough one is beneficial.
- The thickness of the SFMO layer should be much larger than that of the magnetic dead layer at the surface/interface amounting to about 10 nm.
- The presence of a magnetically disordered interface layer, as well as spin-independent tunneling through the barrier layer, deteriorates the TMR.
- The TMR in SFMO-based MTJs may be enhanced by means of (111)-oriented SFMO thin films. This is attributed to the influence of antiphase boundaries on charge carrier scattering in SFMO.

Supplementary Materials: The following are available online at https://www.mdpi.com/article/10.3390/app12052717/s1, Figure S1: AFM image and determination of the surface roughness of a Pt(111) electrode using the software package Gwyddion, Figure S2: AFM images of SFMO thin films deposited by multi-target reactive sputtering at 600 °C taken at three different points with a scan area of 1.05 × 1.05 μm^2, Figure S3: Set of AFM images with different scan size of a SFMO thin film deposited by ceramic target magnetron sputtering and crystallized at 900 °C, Figure S4: Film thickness distribution of a $SrMoO_4$ thin film deposited onto a 150 mm platinized silicon wafer.

Author Contributions: Conceptualization, G.S.; methodology, G.S., N.A.S., and D.A.K.; software, E.A.; validation, G.S. and N.A.S.; formal analysis, E.A.; investigation, G.S., E.A., N.A.S., E.T., N.K., D.A.K., and T.S.I.; resources, E.T., D.A.K., and G.G.; data curation, E.A.; writing—original draft preparation, G.S.; writing—review and editing, G.S. and N.A.S.; visualization, E.A.; supervision, N.A.S. and G.G.; project administration, N.A.S. and G.G.; funding acquisition, N.A.S. All authors have read and agreed to the published version of the manuscript.

Funding: This work was funded by EU project H2020-MSCA-RISE-2017-778308-SPINMULTIFILM. AFM studies were performed at the Center for Shared Use "Material Science and Metallurgy" at the National University of Science and Technology "MISiS" and were supported by the Ministry of Science and Higher Education of the Russian Federation (projects 075-15-2021-696 and FSME-2020-0031 (0718-2020-0031)).

Data Availability Statement: The original contributions presented in the study are included in the article/supplementary material. Further inquiries can be directed to the corresponding author.

Conflicts of Interest: The authors declare no conflict of interest.

References

1. Kobayashi, K.I.; Kimura, T.; Sawada, H.; Terakura, K.; Tokura, Y. Room-Temperature Magnetoresistance in an Oxide Material with an Ordered Double-Perovskite Structure. *Nature* **1998**, *395*, 677–680. [CrossRef]
2. Bibes, M.; Bouzehouane, K.; Barthélémy, A.; Besse, M.; Fusil, S.; Bowen, M.; Seneor, P.; Carrey, J.; Cros, V.; Vaurès, A.; et al. Tunnel Magnetoresistance in Nanojunctions Based on Sr_2FeMoO_6. *Appl. Phys. Lett.* **2003**, *83*, 2629–2631. [CrossRef]
3. Fix, T.; Stoeffler, D.; Henry, Y.; Colis, S.; Dinia, A.; Dimopoulos, T.; Bär, L.; Wecker, J. Diode Effect in All-Oxide Sr_2FeMoO_6-Based Magnetic Tunnel Junctions. *J. Appl. Phys.* **2006**, *99*, 08J107. [CrossRef]
4. Fix, T.; Barla, A.; Ulhaq-Bouillet, C.; Colis, S.; Kappler, J.P.; Dinia, A. Absence of Tunnel Magnetoresistance in Sr_2FeMoO_6-Based Magnetic Tunnel Junctions. *Chem. Phys. Lett.* **2007**, *434*, 276–279. [CrossRef]
5. Asano, H.; Koduka, N.; Imaeda, K.; Sugiyama, M.; Matsui, M. Magnetic and Junction Properties of Half-Metallic Double-Perovskite Thin Films. *IEEE Trans. Magn.* **2005**, *41*, 2811–2813. [CrossRef]
6. Kumar, N.; Misra, P.; Kotnala, R.K.; Gaur, A.; Katiyar, R.S. Room Temperature Magnetoresistance in $Sr_2FeMoO_6/SrTiO_3/Sr_2FeMoO_6$ Trilayer Devices. *J. Phys. D Appl. Phys.* **2014**, *47*, 065006. [CrossRef]
7. Kumar, N.; Misra, P.; Kotnala, R.K.; Gaur, A.; Katiyar, R.S. Growth of Sr_2FeMoO_6 Based Tri-Layer Structure for Room Temperature Magnetoresistive Applications. *Integr. Ferroelectr.* **2014**, *157*, 89–94. [CrossRef]
8. Volkov, N.V. Spintronics: Manganite-based Magnetic Tunnel Structures. *Phys.-Usp.* **2012**, *55*, 250–260. [CrossRef]
9. Butler, W.H.; Zhang, X.-G.; Schulthess, T.C.; MacLaren, J.M. Spin-dependent tunneling conductance of Fe | MgO | Fe sandwiches. *Phys. Rev. B-Condens. Matter Mater. Phys.* **2001**, *63*, 054416. [CrossRef]
10. Zumdahl, S.S. *Chemical Principles*, 5th ed.; Houghton Mifflin: Boston, MA, USA, 2005; pp. 587–590.
11. Nethercot, A.H. Prediction of Fermi Energies and Photoelectric Thresholds Based on Electronegativity Concepts. *Phys. Rev. Lett.* **1974**, *33*, 1088. [CrossRef]
12. Perfetti, P.; Quaresima, C.; Coluzza, C.; Fortunato, C.; Margaritondo, G. Dipole-Induced Changes of the Band Discontinuities at the SiO_2-Si Interface. *Phys. Rev. Lett.* **1986**, *57*, 2065. [CrossRef] [PubMed]

13. Schaeffer, J.K.; Gilmer, D.C.; Capasso, C.; Kalpat, S.; Taylor, B.; Raymond, M.V.; Triyoso, D.; Hegde, R.; Samavedam, S.B.; White, B.E. Application of Group Electronegativity Concepts to the Effective Work Functions of Metal Gate Electrodes on High-κ Gate Oxides. *Microelectron. Eng.* **2007**, *84*, 2196–2200. [CrossRef]
14. Néel, L. Sur Un Nouveau Mode de Couplage Entre Les Aimantations de Deux Couches Minces Ferromagnétiques. *Comptes Rendus Acad. Sci.* **1962**, *255*, 1676–1681.
15. Kools, J.C.S. Effect of Energetic Particle Bombardment during Sputter Deposition on the Properties of Exchange-Biased Spin-Valve Multilayers. *J. Appl. Phys.* **1995**, *77*, 2993. [CrossRef]
16. Kools, J.C.S.; Kula, W.; Mauri, D.; Lin, T. Effect of Finite Magnetic Film Thickness on Néel Coupling in Spin Valves. *J. Appl. Phys.* **1999**, *85*, 4466. [CrossRef]
17. Schrag, B.D.; Anguelouch, A.; Ingvarsson, S.; Xiao, G.; Lu, Y.; Trouilloud, P.L.; Gupta, A.; Wanner, R.A.; Gallagher, W.J.; Rice, P.M.; et al. Néel "Orange-Peel" Coupling in Magnetic Tunnelling Junction Devices. *Appl. Phys. Lett.* **2000**, *77*, 2373. [CrossRef]
18. Kim, K.Y.; Jang, S.H.; Shin, K.H.; Kim, H.J.; Kang, T. Interlayer Coupling Field in Spin Valves with CoFe/Ru/CoFe/FeMn Synthetic Antiferromagnets (Invited). *J. Appl. Phys.* **2001**, *89*, 7612. [CrossRef]
19. Chopra, H.D.; Yang, D.X.; Chen, P.; Parks, D.; Egelhoff, W. Nature of Coupling and Origin of Coercivity in Giant Magnetoresistance NiO-Co-Cu-Based Spin Valves. *Phys. Rev. B-Condens. Matter Mater. Phys.* **2000**, *61*, 9642. [CrossRef]
20. Yao, X.; Schneider, C.W.; Lippert, T.; Wokaun, A. Manipulation of Ion Energies in Pulsed Laser Deposition to Improve Film Growth. *Appl. Phys. A Mater. Sci. Process.* **2019**, *125*, 344. [CrossRef]
21. Welzel, T.; Kleinhempel, R.; Dunger, T.; Richter, F. Ion Energy Distributions in Magnetron Sputtering of Zinc Aluminium Oxide. *Plasma Process. Polym.* **2009**, *6*, S331–S336. [CrossRef]
22. Suchaneck, G.; Kalanda, N.; Artsiukh, E.; Gerlach, G. Challenges in $Sr_2FeMoO_{6-\delta}$ Thin Film Deposition. *Phys. Status Solidi Basic Res.* **2019**, *257*, 1900312. [CrossRef]
23. Moritz, J.; Garcia, F.; Toussaint, J.C.; Dieny, B.; Nozières, J.P. Orange Peel Coupling in Multilayers with Perpendicular Magnetic Anisotropy: Application to (Co/Pt)-Based Exchange-Biased Spin-Valves. *Europhys. Lett.* **2004**, *65*, 123. [CrossRef]
24. Kuznetsov, M.A.; Udalov, O.G.; Fraerman, A.A. Anisotropy of Neel "Orange-Peel" Coupling in Magnetic Multilayers. *J. Magn. Magn. Mater.* **2019**, *474*, 104–106. [CrossRef]
25. Nečas, D.; Klapetek, P. Gwyddion: An Open-Source Software for SPM Data Analysis. *Cent. Eur. J. Phys.* **2012**, *10*, 181–188. [CrossRef]
26. Duparré, A.; Ferre-Borrull, J.; Gliech, S.; Notni, G.; Steinert, J.; Bennett, J.M. Surface Characterization Techniques for Determining the Root-Mean-Square Roughness and Power Spectral Densities of Optical Components. *Appl. Opt.* **2002**, *41*, 154–171. [CrossRef] [PubMed]
27. Palasantzas, G. Roughness Spectrum and Surface Width of Self-Affine Fractal Surfaces via the k-Correlation Model. *Phys. Rev. B* **1993**, *48*, 11472. [CrossRef] [PubMed]
28. Church, E.L.; Takacs, P.Z. Optimal Estimation of Finish Parameters. In Proceedings of the Proc. SPIE 1530, Optical Scatter: Applications, Measurement, and Theory, San Diego, CA, USA, 24–26 July 1991; Stover, J.C., Ed.; pp. 71–85. [CrossRef]
29. Buijnsters, J.G.; Camero, M.; Vázquez, L. Growth Dynamics of Ultrasmooth Hydrogenated Amorphous Carbon Films. *Phys. Rev. B-Condens. Matter Mater. Phys.* **2006**, *74*, 155417. [CrossRef]
30. Tegen, S.; Mönch, I.; Schumann, J.; Vinzelberg, H.; Schneider, C.M. Effect of Néel Coupling on Magnetic Tunnel Junctions. *J. Appl. Phys.* **2001**, *89*, 8169. [CrossRef]
31. Roy, S.; Dubenko, I.; Edorh, D.D.; Ali, N. Size Induced Variations in Structural and Magnetic Properties of Double Exchange $La_{0.8}Sr_{0.2}MnO_{3-\delta}$ Nano-Ferromagnet. *J. Appl. Phys.* **2004**, *96*, 1202. [CrossRef]
32. Liebermann, L.N.; Fredkin, D.R.; Shore, H.B. Two-Dimensional "Ferromagnetism" in Iron. *Phys. Rev. Lett.* **1969**, *22*, 539. [CrossRef]
33. Liebermann, L.; Clinton, J.; Edwards, D.M.; Mathon, J. "Dead" Layers in FM Transition Metals. *Phys. Rev. Lett.* **1970**, *25*, 232. [CrossRef]
34. Gangopadhyay, S.; Hadjipanayis, G.C.; Dale, B.; Sorensen, C.M.; Klabunde, K.J.; Papaefthymiou, V.; Kostikas, A. Magnetic Properties of Ultrafine Iron Particles. *Phys. Rev. B* **1992**, *45*, 9778. [CrossRef] [PubMed]
35. Popova, E.; Keller, N.; Gendron, F.; Guyot, M.; Brianso, M.C.; Dumond, Y.; Tessier, M. Structure and Magnetic Properties of Yttrium-Iron-Garnet Thin Films Prepared by Laser Deposition. *J. Appl. Phys.* **2001**, *90*, 1422. [CrossRef]
36. Aeschlimann, R.; Preziosi, D.; Scheiderer, P.; Sing, M.; Valencia, S.; Santamaria, J.; Luo, C.; Ryll, H.; Radu, F.; Claessen, R.; et al. A Living-Dead Magnetic Layer at the Surface of Ferrimagnetic $DyTiO_3$ Thin Films. *Adv. Mater.* **2018**, *30*, 1707489. [CrossRef]
37. Angeloni, M.; Balestrino, G.; Boggio, N.G.; Medaglia, P.G.; Orgiani, P.; Tebano, A. Suppression of the Metal-Insulator Transition Temperature in Thin $La_{0.7}Sr_{0.3}MnO_3$ Films. *J. Appl. Phys.* **2004**, *96*, 6387. [CrossRef]
38. Huijben, M.; Martin, L.W.; Chu, Y.H.; Holcomb, M.B.; Yu, P.; Rijnders, G.; Blank, D.H.A.; Ramesh, R. Critical Thickness and Orbital Ordering in Ultrathin $La_{0.7}Sr_{0.3}MnO_3$ Films. *Phys. Rev. B-Condens. Matter Mater. Phys.* **2008**, *78*, 094413. [CrossRef]
39. Mottaghi, N.; Seehra, M.S.; Trappen, R.; Kumari, S.; Huang, C.Y.; Yousefi, S.; Cabrera, G.B.; Romero, A.H.; Holcomb, M.B. Insights into the Magnetic Dead Layer in $La_{0.7}Sr_{0.3}MnO_3$ Thin Films from Temperature, Magnetic Field and Thickness Dependence of Their Magnetization. *AIP Adv.* **2018**, *8*, 056319. [CrossRef]
40. Julliere, M. Tunnelling between FM Films. *Phys. Lett. A* **1975**, *54*, 225–226. [CrossRef]
41. Shang, C.H.; Nowak, J.; Jansen, R.; Moodera, J.S. Temperature Dependence of Magnetoresistance and Surface Magnetization in FM Tunnel Junctions. *Phys. Rev. B-Condens. Matter Mater. Phys.* **1998**, *58*, R2917–R2920. [CrossRef]

42. Pierce, D.T.; Celotta, R.J.; Unguris, J.; Siegmann, H.C. Spin-Dependent Elastic Scattering of Electrons from a FM Glass, $Ni_{40}Fe_{40}B_{20}$. *Phys. Rev. B* **1982**, *26*, 2566–2574. [CrossRef]
43. Mauri, D.; Scholl, D.; Siegmann, H.C.; Kay, E. Observation of the Exchange Interaction at the Surface of a Ferromagnet. *Phys. Rev. Lett.* **1988**, *61*, 758–761. [CrossRef] [PubMed]
44. Kou, X.; Schmalhorst, J.; Thomas, A.; Reiss, G. Temperature Dependence of the Resistance of Magnetic Tunnel Junctions with MgO Barrier. *Appl. Phys. Lett.* **2006**, *88*, 212115. [CrossRef]
45. Slonczewski, J.C. Conductance and Exchange Coupling of Two Ferromagnets Separated by a Tunnelling Barrier. *Phys. Rev. B* **1989**, *39*, 6995. [CrossRef] [PubMed]
46. Stearns, M.B. Simple Explanation of Tunnelling Spin-Polarization of Fe, Co, Ni and Its Alloys. *J. Magn. Magn. Mater.* **1977**, *5*, 167–171. [CrossRef]
47. Pickett, W.E.; Singh, D.J. Transport and Fermiology of the FM Phase of $La_{2/3}A_{1/3}MnO_3$ (A = Ca, Sr, Ba). *J. Magn. Magn. Mater.* **1997**, *172*, 237–246. [CrossRef]
48. Yamada, M.G.; Jackeli, G. Magnetic and Electronic Properties of Spin-Orbit Coupled Dirac Electrons on a (001) Thin Film of Double-Perovskite Sr_2FeMoO_6. *Phys. Rev. Mater.* **2020**, *4*, 074007. [CrossRef]
49. Hwang, H.Y.; Cheong, S.; Ong, N.P.; Batlogg, B. Spin-Polarized Intergrain Tunnelling in $La_{2/3}Sr_{1/3}MnO_3$. *Phys. Rev. Lett.* **1996**, *77*, 2041–2044. [CrossRef]
50. Niebieskikwiat, D.; Caneiro, A.; Sánchez, R.D.; Fontcuberta, J. Oxygen-Induced Grain Boundary Effects on Magnetotransport Properties of $Sr_2FeMoO_{6+\delta}$. *Phys. Rev. B-Condens. Matter Mater. Phys.* **2001**, *64*, 180406. [CrossRef]
51. Sarma, D.D.; Ray, S.; Tanaka, K.; Kobayashi, M.; Fujimori, A.; Sanyal, P.; Krishnamurthy, H.R.; Dasgupta, C. Intergranular Magnetoresistance in Sr_2FeMoO_6 from a Magnetic Tunnel Barrier Mechanism across Grain Boundaries. *Phys. Rev. Lett.* **2007**, *98*, 157205. [CrossRef]
52. Wang, J.F.; Li, Z.; Xu, X.J.; Gu, Z.B.; Yuan, G.L.; Zhang, S.T. The Competitive and Combining Effects of Grain Boundary and Fe/Mo Antisite Defects on the Low-Field Magnetoresistance in Sr_2FeMoO_6. *J. Am. Ceram. Soc.* **2014**, *97*, 1137–1142. [CrossRef]
53. García-Hernández, M.; Martínez, J.L.; Martínez-Lope, M.J.; Casais, M.T.; Alonso, J.A. Finding Universal Correlations between Cationic Disorder and Low Field Magnetoresistance in FeMo Double Perovskite Series. *Phys. Rev. Lett.* **2001**, *88*, 2443. [CrossRef] [PubMed]
54. Tomioka, Y.; Okuda, T.; Okimoto, Y.; Kumai, R.; Kobayashi, K.; Tokura, Y. Magnetic and Electronic Properties of a Single Crystal of Ordered Double Perovskite. *Phys. Rev. B-Condens. Matter Mater. Phys.* **2000**, *61*, 422. [CrossRef]
55. Yin, H.Q.; Zhou, J.S.; Dass, R.; Zhou, J.P.; McDevitt, J.T.; Goodenough, J.B. Intra- versus intergranular low-field magnetoresistance of Sr_2FeMoO_6 thin films. *Appl. Phys. Lett.* **1999**, *75*, 2812. [CrossRef]
56. Shinde, S.R.; Ogale, S.B.; Greene, R.L.; Venkatesan, T.; Tsoi, K.; Cheong, S.W.; Millis, A.J. Thin Films of Double Perovskite Sr_2FeMoO_6: Growth, Optimization, and Study of the Physical and Magnetotransport Properties of Films Grown on Single-Crystalline and Polycrystalline $SrTiO_3$ Substrates. *J. Appl. Phys.* **2003**, *93*, 1605–1612. [CrossRef]
57. Saloaro, M.; Majumdar, S.; Huhtinen, H.; Paturi, P. Absence of Traditional Magnetoresistivity Mechanisms in Sr_2FeMoO_6 Thin Films Grown on $SrTiO_3$, MgO and $NdGaO_3$ Substrates. *J. Phys. Condens. Matter* **2012**, *24*, 366003. [CrossRef]
58. Sanchez, D.; Auth, N.; Jakob, G.; Martínez, J.L.; García-Hernández, M. Pulsed Laser Deposition of Sr_2FeMoO_6 Thin Films. *J. Magn. Magn. Mater.* **2005**, *294*, e119. [CrossRef]
59. Metsänoja, M.; Majumdar, S.; Huhtinen, H.; Paturi, P. Effect of Ex Situ Post-Annealing Treatments on Sr_2FeMoO_6 Thin Films. *J. Supercond. Nov. Magn.* **2012**, *25*, 829–833. [CrossRef]
60. Manako, T.; Izumi, M.; Konishi, Y.; Kobayashi, K.I.; Kawasaki, M.; Tokura, Y. Epitaxial Thin Films of Ordered Double Perovskite Sr_2FeMoO_6. *Appl. Phys. Lett.* **1999**, *74*, 2215–2217. [CrossRef]
61. Arora, S.K.; Sofin, R.G.S.; Shvets, I.V. Magnetoresistance Enhancement in Epitaxial Magnetite Films Grown on Vicinal Substrates. *Phys. Rev. B-Condens. Matter Mater. Phys.* **2005**, *72*, 134404. [CrossRef]
62. Chang, J.; Park, Y.S.; Kim, S.K. Atomically Flat Single-Terminated $SrTiO_3$ (111) Surface. *Appl. Phys. Lett.* **2008**, *92*, 152910. [CrossRef]
63. Hu, Y.C.; Ge, J.J.; Ji, Q.; Lv, B.; Wu, X.S.; Cheng, G.F. Synthesis and Crystal Structure of Double-Perovskite Compound Sr_2FeMoO_6. *Powder Diffr.* **2010**, *25*, S17–S21. [CrossRef]
64. Garcia, V.; Bibes, M.; Barthélémy, A.; Bowen, M.; Jacquet, E.; Contour, J.P.; Fert, A. Temperature Dependence of the Interfacial Spin Polarization of $La_{2/3}Sr_{1/3}MnO_3$. *Phys. Rev. B-Condens. Matter Mater. Phys.* **2004**, *69*, 052403. [CrossRef]
65. Jo, M.H.; Mathur, N.D.; Evetts, J.E.; Blamire, M.G.; Bibes, M.; Fontcuberta, J. Inhomogeneous Transport in Heteroepitaxial $La_{0.7}Ca_{0.3}MnO_3/SrTiO_3$ Multilayers. *Appl. Phys. Lett.* **1999**, *75*, 3689. [CrossRef]
66. LeClair, P.; Swagten, H.J.M.; Kohlhepp, J.T.; Van De Veerdonk, R.J.M.; De Jonge, W.J.M. Apparent Spin Polarization Decay in Cu-Dusted $Co/Al_2O_3/Co$ Tunnel Junctions. *Phys. Rev. Lett.* **2000**, *84*, 2933. [CrossRef] [PubMed]
67. Bibes, M.; Valencia, S.; Balcells, L.; Martínez, B.; Fontcuberta, J.; Wojcik, M.; Nadolski, S.; Jedryka, E. Charge Trapping in Optimally Doped Epitaxial Manganite Thin Films. *Phys. Rev. B-Condens. Matter Mater. Phys.* **2002**, *66*, 134416. [CrossRef]
68. Izumi, M.; Ogimoto, Y.; Okimoto, Y.; Manako, T.; Ahmet, P.; Nakajima, K.; Chikyow, T.; Kawasaki, M.; Tokura, Y. Insulator-Metal Transition Induced by Interlayer Coupling in $La_{0.6}Sr_{0.4}MnO_3/SrTiO_3$ Superlattices. *Phys. Rev. B-Condens. Matter Mater. Phys.* **2001**, *64*, 064429. [CrossRef]
69. Zhang, X.G.; Butler, H.; Bandyopadhyay, A. Effects of the Iron-Oxide Layer in Fe-FeO-MgO-Fe Tunnelling Junctions. *Phys. Rev. B-Condens. Matter Mater. Phys.* **2003**, *68*, 092402. [CrossRef]

70. Zermatten, P.J.; Bonell, F.; Andrieu, S.; Chshiev, M.; Tiusan, C.; Schuhl, A.; Gaudin, G. Influence of Oxygen Monolayer at Fe/MgO Interface on Transport Properties in Fe/MgO/Fe(001) Magnetic Tunnel Junctions. *Appl. Phys. Express* **2012**, *5*, 023001. [CrossRef]
71. Kircheisen, R.; Töpfer, J. Nonstoichiometry, Point Defects and Magnetic Properties in $Sr_2FeMoO_{6-\delta}$ Double Perovskites. *J. Solid State Chem.* **2012**, *185*, 76–81. [CrossRef]
72. Yuasa, S.; Nagahama, T.; Fukushima, A.; Suzuki, Y.; Ando, K. Giant Room-Temperature Magnetoresistance in Single-Crystal Fe/MgO/Fe Magnetic Tunnel Junctions. *Nat. Mater.* **2004**, *3*, 868–871. [CrossRef]
73. Daughton, J.M. Magnetic Tunnelling Applied to Memory (Invited). *J. Appl. Phys.* **1997**, *81*, 3758. [CrossRef]
74. Parkin, S.S.P.; Kaiser, C.; Panchula, A.; Rice, P.M.; Hughes, B.; Samant, M.; Yang, S.H. Giant Tunnelling Magnetoresistance at Room Temperature with MgO (100) Tunnel Barriers. *Nat. Mater.* **2004**, *3*, 862–867. [CrossRef]
75. Yuasa, S.; Fukushima, A.; Kubota, H.; Suzuki, Y.; Ando, K. Giant Tunnelling Magnetoresistance up to 410% at Room Temperature in Fully Epitaxial Co/MgO/Co Magnetic Tunnel Junctions with Bcc Co(001) Electrodes. *Appl. Phys. Lett.* **2006**, *89*, 042505. [CrossRef]
76. Angervo, I.; Saloaro, M.; Palonen, H.; Majumdar, S.; Huhtinen, H.; Paturi, P. Thickness Dependent Properties of Sr_2FeMoO_6 Thin Films Grown on $SrTiO_3$ and $(LaAlO_3)_{0.3}(Sr_2AlTaO_6)_{0.7}$ Substrates. *Phys. Procedia* **2015**, *75*, 1011–1021. [CrossRef]
77. Bibes, M.; Balcells, L.; Valencia, S.; Fontcuberta, J.; Wojcik, M.; Jedryka, E.; Nadolski, S. Nanoscale Multiphase Separation at $La_{2/3}Ca_{1/3}MnO_3/SrTiO_3$ Interfaces. *Phys. Rev. Lett.* **2001**, *87*, 067210. [CrossRef] [PubMed]
78. Sidorenko, A.A.; Allodi, G.; De Renzi, R.; Balestrino, G.; Angeloni, M. Mn^{55} NMR and Magnetization Studies of $La_{0.67}Sr_{0.33}MnO_3$ Thin Films. *Phys. Rev. B-Condens. Matter Mater. Phys.* **2006**, *73*, 054406. [CrossRef]
79. Speriosu, V.S.; Nozieres, J.P.; Gurney, B.A.; Dieny, B.; Huang, T.C.; Lefakis, H. Role of Interfacial Mixing in Giant Magnetoresistance. *Phys. Rev. B* **1993**, *47*, 11579. [CrossRef]
80. Schnittger, S.; Jooss, C.; Sievers, S. Magnetic and Structural Properties of Cobalt Ferrite Thin Films and Structures. *J. Phys. Conf. Ser.* **2010**, *200*, 072086. [CrossRef]
81. Wakabayashi, Y.K.; Nonaka, Y.; Takeda, Y.; Sakamoto, S.; Ikeda, K.; Chi, Z.; Shibata, G.; Tanaka, A.; Saitoh, Y.; Yamagami, H.; et al. Electronic Structure and Magnetic Properties of Magnetically Dead Layers in Epitaxial $CoFe_2O_4/AL_2O_3/Si(111)$ Films Studied by x-Ray Magnetic Circular Dichroism. *Phys. Rev. B* **2017**, *96*, 104410. [CrossRef]
82. Miao, G.-X.; Moodera, J.S. Numerical Evaluations on the Asymmetric Bias dependence of Magnetoresistance in Double Spin Filter Tunnel Junctions. *J. Appl. Phys.* **2009**, *106*, 023911. [CrossRef]
83. Panguluri, R.P.; Xu, S.; Moritomo, Y.; Solovyev, I.V.; Nadgorny, B. Disorder Effects in Half-Metallic Sr_2FeMoO_6 Single Crystals. *Appl. Phys. Lett.* **2009**, *94*, 012501. [CrossRef]
84. Serrate, D.; De Teresa, J.M.; Algarabel, P.A.; Ibarra, M.R.; Galibert, J. Intergrain Magnetoresistance up to 50 T in the Half-Metallic $(Ba_{0.8}Sr_{0.2})_2FeMoO_6$ Double Perovskite: Spin-Glass Behavior of the Grain Boundary. *Phys. Rev. B-Condens. Matter Mater. Phys.* **2005**, *71*, 104409. [CrossRef]
85. Miller, C.W.; Schuller, I.K.; Dave, R.W.; Slaughter, J.M.; Zhou, Y.; Åkerman, J. Temperature and Angular Dependences of Dynamic Spin-Polarized Resonant Tunnelling in CoFeB/MgO/NiFe Junctions. *J. Appl. Phys.* **2008**, *103*, 07A904. [CrossRef]
86. Bratkovsky, A.M. Tunnelling of electrons in conventional and half-metallic systems: Towards very large magnetoresistance. *Phys. Rev. B* **1997**, *56*, 2344. [CrossRef]
87. Xu, Y.; Matsuda, A.; Beasley, M.R. Role of Inelastic Effects on Tunnelling via Localized States in Metal-Insulator-Metal Tunnel Junctions. *Phys. Rev. B* **1990**, *42*, 1492. [CrossRef]
88. Suchaneck, G.; Artiukh, E. Magnetoresistance of Antiphase Boundaries in $Sr_2FeMoO_{6-\delta}$. *Phys. Status Solidi* **2021**, 2100353. [CrossRef]
89. Moritomo, Y.; Xu, S.; Machida, A.; Akimoto, T.; Nishibori, E.; Takata, M.; Sakata, M.; Ohoyama, K. Crystal and Magnetic Structure of Conducting Double Perovskite Sr_2FeMoO_6. *J. Phys. Soc. Jpn.* **2000**, *69*, 1723–1726. [CrossRef]